Revision 2

Word count: 9548

Raman scattering of omphacite at high pressure: towards its possible application to elastic geothermobarometry

Lisa Baratelli[1], Mara Murri[2], Matteo Alvaro[2], Mauro Prencipe[3], Boriana Mihailova[4], Fernando Cámara[1]

[1]Department of Earth Sciences, University of Milan, Via Sandro Botticelli 23, 20133 Milan, Italy.

[2]Department of Earth and Environmental Sciences, University of Pavia, Via Adolfo Ferrata 1, 27100 Pavia, Italy.

[3]Department of Earth Sciences, University of Turin, Via Valperga Caluso 35, 10125, Turin, Italy.

[4]Department of Earth Sciences, Universität Hamburg, Grindelallee 48, 20146 Hamburg, Germany.

Corresponding author: Lisa Baratelli. Contact: lisa.baratelli@unimi.it

Abstract

Due to their widespread occurrence in several geological settings, omphacite inclusions could be used for elastic Raman geothermobarometry. However, the Raman scattering of complex silicate minerals entrapped in a host depends on both the chemical composition and elastic strain developed during the metamorphic pathway, which makes the task very challenging. Here, as a very first step to probe the potential of omphacite to be used as a mineral inclusion in elastic geothermobarometry, we report the pressure dependence of the Raman spectra of omphacite crystals with the same composition, approximately $Jd_{45}Di_{55}$, but having different symmetry because of the existence ($P2/n$) or absence ($C2/c$) of chemical order at the six- and eight-coordinated cation sites. The experimental results are complemented by ab initio quantum

mechanical simulations on fully ordered omphacite ($Jd_{50}Di_{50}$). We demonstrate that the position of the well-resolved Raman peak near 688 cm^{-1}, arising from Si-O-Si bond bending, is very sensitive to pressure but independent of the state of chemical order, which makes it promising to be utilized in Raman geobarometry. The width of this peak varies with chemical order but not with pressure and therefore can be used to constrain the temperature of inclusion entrapment, because the chemical order is indicative of the closure temperature of the cation-exchange reaction. However, further detailed analyses on the compositional variation of the Raman spectra of omphacite is required before considering omphacite-in-garnet systems as suitable for Raman elastic geothermobarometry.

Keywords: Omphacite, site-occupancy order, Raman spectroscopy, high pressure, ab initio calculation

Introduction

Clinopyroxenes (general formula $M2M1T_2O_6$) are key minerals, due to their widespread occurrence in the Earth's crust and upper mantle (Skelton and Walker 2015), to characterize various geological settings and processes. They can be found as both rock-forming and accessory minerals in several terrestrial rock types from diverse geological contexts, including mantle xenoliths, magmatic rocks (e.g., Lentz et al. 2011; Murri et al. 2016, 2019b; Gianola et al. 2023) and high-pressure/temperature metamorphic rocks (Philpotts and Ague 2009; Gilio et al. 2020). Clinopyroxenes also occur as inclusions in diamonds (Meyer and Boyd 1972; Nestola et al. 2016; Pasqualetto et al. 2022) and as rock-forming minerals in meteorites (e.g., Papike 1980; Alvaro et al. 2015; Carli et al. 2023). Among clinopyroxenes, omphacite, a solid solution of jadeite ($NaAlSi_2O_6$) (20-80%), augite [$Ca(Mg,Fe^{2+})Si_2O_6$] (20-80%), and aegirine ($NaFe^{3+}Si_2O_6$) (0-50%)

(Morimoto 1988) with the general formula $(Ca,Na)(Mg,Fe^{2+},Al)Si_2O_6$, is extremely important for constraining pressure and temperature conditions in eclogitic metabasites where quartz is not present as an equilibrium phase at peak conditions. It is well known that omphacites may exhibit site-occupancy cation order, which leads to a splitting of both M1 and M2 sites into (M1, M11) and (M2, M21), respectively (Figure 1). Consequently, the chemical order reduces the space group symmetry from *C*2/*c* to *P*2/*n*, (e.g., Carpenter et al. 1990a, b; Boffa Ballaran et al. 1998a, b). Thus, the determination of the state of chemically ordered omphacite can constrain the closure temperature and cooling rate experienced by the host rock. The degree of cation order of omphacite is commonly determined by means of single-crystal X-ray diffraction (XRD) measurements followed by structural refinements, but this analysis generally requires large (~50-150 μm) good-quality single crystals. Moreover, chemically ordered regions form antiphase domains that are detectable by transmission electron microscopy, therefore their size variation has been proposed to serve as a geothermometer (Phakey and Ghose 1973; Carpenter 1980, 1981a, b). However, the dimensions of chemically ordered regions depend also on the chemical composition as well (Cámara et al. 1998) and they can be further affected by post-crystallization deformation processes (Van Roermund and Lardeaux 1991). Raman spectroscopy can verify the existence of M-site cation order in omphacite by the splitting of the SiO_4-stretching Raman peak near 1017 cm^{-1}, due to the doubling of the primitive unit cell (Katerinopoulou et al. 2008). Besides, Raman spectroscopy has the advantage to probe micrometer-size spatial regions without the necessity to extract the crystal from the host. Consequently, this analytical method is among the most popular experimental techniques used in elastic geothermobarometry (Korsakov et al. 2009; Anzolini et al. 2018; Nestola et al. 2018; Zhong et al. 2019; Campomenosi et al. 2021). By using this technique, it is possible to estimate the equilibration pressure and temperature of a mineral. The pressure and temperature conditions of the inclusion entrapment (P-T_{trap}) can be estimated

knowing the inclusion pressure (P_{inc}) at the conditions at which it is exhumed to the surface (P-T_{end}) and the elastic properties of the host and the inclusion, that allow to calculate isomekes (Gilio et al. 2021). An isomeke is a line in the pressure-temperature space along which the volume strain of the inclusion and the surrounding host are the same (Campomenosi et al. 2022). Then, isomekes are used to determine the over- or under-pressure conditions developed in the inclusion, and, therefore, the final inclusion pressure. Thus, to utilize omphacite inclusions as geothermobarometry markers in metamorphic rocks, detailed analyses of the atomic dynamics of omphacite as a function of chemical composition, temperature and pressure is required. However, Raman-scattering data on omphacite are available only at ambient conditions, mainly in comparison with other chain silicates (Buzatu and Buzgar 2010; Andò and Garzanti 2014; Franz et al. 2014).

Here, as a very first step to probe the potential of omphacite to be used as a mineral inclusion in elastic geothermobarometry, we report the Raman spectra of omphacite crystals with and without *M*-site cation order, while having the same composition ~$Jd_{45}Di_{55}$, at pressures up to ~10 GPa, along with Hartree-Fock/Density-Functional-Theory (HF/DFT) simulations on fully ordered $Jd_{50}Di_{50}$ omphacite in the same pressure range.

Materials and methods

Sample description

We used omphacite crystals from Münchberg Mass, Bavaria (Matthes and Schmidt 1974; O'Brien 1993), which belong to the same omphacite sample that has been previously analyzed with infrared spectroscopy by Boffa Ballaran et al. (1998a, b) (sample 74AM41) and by high-pressure single-crystal XRD by Pandolfo et al. (2012a, b). We selected single crystals with low iron content to avoid further chemical effects on the Raman spectra (Katerinopoulou et al. 2008). For

in situ high-pressure Raman spectroscopic measurements, we used two natural samples (natural-8 and natural-11), which exhibited a high degree of cation order (Boffa Ballaran et al. 1998a), and two samples annealed at 1173 K for 168 h (annealed-3 and annealed-7) to achieve a state of long-range cation disorder. The size of samples natural-8, natural-11 and annealed-3 was approximately 90×150×200 μm^3, whereas size of sample annealed-7 was ~50×50×60 μm^3.

Chemical composition

Wavelength-dispersive electron microprobe analyses (EMPA) were performed on the very same specimens used in the high-pressure Raman-scattering experiments. After conducting the Raman experiments, the omphacite crystals were embedded into epoxy resin, polished, and carbon coated for electron microprobe analyses. The chemical composition was determined with a Jeol 8200 Super Probe electron microprobe at the Department of Earth Sciences of the University of Milan, operating at an acceleration voltage of 15 kV and beam current of 5 nA (beam size = 3 μm). A ZAF correction (Z = atomic number, A = absorption coefficient, F = fluorescence coefficient), using the PAP routine (Pouchou and Pichoir 1985) was applied. Standards, spectral lines, and analytical crystals used were: grossular (Si, Al*K*α, TAP; Ca*K*α, PET), ilmenite (Ti*K*α, PET), metallic Cr (Cr*K*α, LIF), fayalite (Fe*K*α, LIF), rhodonite (Mn*K*α, LIF), forsterite (Mg*K*α, TAP), omphacite (Na*K*α, TAP) and K-feldspar (K*K*α, PET).

Single-crystal X-ray diffraction

Single-crystal XRD experiments were performed at the Department of Earth Sciences of the University of Milan to determine the degree of long-range M-site cation ordering in the crystals selected for high-pressure Raman spectroscopy. Samples natural-8, natural-11, annealed-3 were analyzed with a Xcalibur-1-Oxford diffractometer equipped with a Mo*K*α sealed tube source and a

charge-coupled device (CCD) detector. Due to its smaller size (see above), sample annealed-7 was analyzed with a Rigaku XtaLAB Synergy-S diffractometer equipped with a HyPix-6000HE HPC area detector, using a monochromatic X-ray incident beam with an energy of 17.4 keV (λ=0.71073 Å, i.e., Mo*K*α), which is characterized by a higher brilliance. Structure refinements were performed using the program SHELXL (Sheldrick 2015). The structure of ordered and disordered omphacite was refined in *P*2/*n* and *C*2/*c* space groups, respectively, starting from the models provided by Pavese et al. (2000) and McCormick (1986). Scattering curves were taken from *the International Tables for Crystallography* (Wilson 1995). Neutral vs. ionized scattering factors were used to refine the occupancy for all sites that are not involved in chemical substitutions (i.e. O sites and ^{T1}Si in *P*2/*n*) (Hawthorne et al. 1995), while scattering factors of ionized atoms were used for ^{T2}Si and the six-coordinated M1 and M11 sites alongside the eight-coordinated M2 and M21 sites. The site partitioning was obtained using the refinement model proposed by Boffa Ballaran et al. (1998a) and the chemical constraints from our EMPA data. Crystallographic information files (CIFs) are available as Online Materials.

High-pressure Raman spectroscopy

Raman spectra of the four selected crystals were collected using a Horiba Jobin-Yvon S.A.S. T64000 triple monochromator spectrometer at the Mineralogisch-Petrographisches Institut, Universität Hamburg, equipped with an Olympus BX41 confocal microscope and a Symphony liquid-N_2-cooled CCD detector. Raman scattering was excited with the 514.532-nm or the 488.0-nm lines of a Coherent Innova 90C Fred Ar^+ laser, using an Olympus LM Plan FLN 50× long-working distance objective with a numerical aperture of 0.5. The spectrometer was calibrated to the T_{2g} mode at 520.5 cm^{-1} of a Si wafer. The spectral resolution was ~2 cm^{-1}, while the instrumental accuracy in determining the peak position was ~0.35 cm^{-1}.

In situ high-pressure Raman experiments were conducted with Boehler-Almax diamond anvil cells equipped with diamonds with a culet diameter of 600 μm. The sample chamber was made by a stainless-steel gasket with a thickness of 0.25 mm, which was initially indented to ~ 95 μm and then drilled with an Almax-easyLab spark eroder with tungsten carbide tips, to obtain a hole with a diameter of 300 μm. A 16:3:1 methanol–ethanol–water mixture was used as a pressure-transmitting medium, which remains hydrostatic up to 10.5 GPa (Angel et al. 2007). The pressure P was determined via the ruby photoluminescence R1 line (Munro et al. 1985) with a precision of ~ 0.1 GPa.

Parallel polarized Raman spectra (polarization of incident light $\mathbf{E}_i$ parallel to the polarization of the scattered light $\mathbf{E}_s$) were collected in the range 50-1250 cm^{-1} with acquisition times of 60 or 180 s averaged over three accumulations. The variations in the relative intensities indicated that the samples were oriented with the crystallographic **c** axis approximately parallel (natural-8 and annealed-3) or perpendicular (natural-11 and annealed-7) to $\mathbf{E}_i$; the orientational dependence of the Raman intensities was established by measuring an omphacite grain for which single-crystal XRD showed that the prism axis coincides with the crystallographic **c** axis. In both cases, the direction of the propagation of the incident light $\mathbf{k}_i$ was $\perp$ to **c**. Therefore, in (**c** || $\mathbf{E}_i$ || $\mathbf{E}_s$) scattering geometry the Raman scattering is dominated by the (zz)-component of the Raman polarizability tensor, whereas in (**c** $\perp$ $\mathbf{E}_i$ || $\mathbf{E}_s$) scattering geometry the Raman spectrum is determined by (xx)- and/or (yy)-components of the polarizability tensor, depending on the orientation of the **b** axis with respect to $\mathbf{k}_i$. At each pressure step, the Raman scattering from the diamond anvils was collected to estimate the degree of depolarization of Raman scattering due to stress-induced changes in the optical properties of the diamond anvils (Mihailova et al. 2019). In addition, a background spectrum was measured aside from the sample while keeping the same focus, and subsequently subtracted from the sample spectrum to eliminate the contribution from

the pressure-transmitting medium. Then the spectra were reduced by the Bose-Einstein population factor to account for the temperature dependence of the Raman intensities, using the relation: $I_{reduced} = I_{measured}/[(e^{\hbar\omega/k_BT} - 1)^{-1} + 1]$, where $\hbar$, k_B, ω, and T are the reduced Planck's constant, Boltzmann's constant, phonon angular frequency (in s^{-1}) and temperature (in K), respectively. The peak positions, full widths at half maximum (FWHMs) and integrated intensities were determined by fitting the temperature-reduced spectra with pseudo-Voigt peak-shape functions $PV=qL+(1-q)G$, where L and G are Lorentzian and Gaussian functions and q is a variable weighting coefficient. The OriginLab 2022 software package was used for data evaluation.

Computational methods

Ab initio hybrid HF/DFT simulations have been conducted with the CRYSTAL17 software (Dovesi et al. 2018) by using the WC1LYP functional. This functional has been shown to correctly reproduce the elastic and vibrational properties of crystals (e.g. Prencipe et al. 2011, 2012; Prencipe 2012, 2018; Stangarone et al. 2016). The WC1LYP functional is based on the generalized gradient approximation (GGA) exchange functional WC (Wu and Cohen 2006), mixed with 16% of the exact *non-local* Hartree-Fock exchange, and the Lee-Yan-Parr (LYP) correlation functional (Lee et al. 1988). The grid for the numerical evaluation of the DFT exchange-correlation functionals was chosen by the keyword XLGRID of CRYSTAL17 (Dovesi et al. 2018) and corresponds to a total of 900,780 points in the unit cell. A measure of the numerical accuracy provided by such a grid is the evaluation of the total number of electrons in the unit cell, by the numerical integration of the electron density over the cell volume. For omphacite, we obtained 415.99999 electrons out of 416 for the reference volume at the static limit (no zero-point and thermal pressures due to vibrational effects included, see Prencipe et al. 2011) and at a static pressure of 0 GPa. The localized contracted atomic basis sets used were: Na 8-511(1d)G; Al 85-11(1d)G; Ca 865-11(3d)G; Mg 85-

11(1d)G; Si 88-31(1d)G; O 84-11(1d1d)G (Sophia et al. 2014; Valenzano et al. 2006). Within the CRYSTAL code, the accuracy in evaluating the Coulomb and Hartree-Fock exchange series is controlled by the keyword TOLINTEG, for which we set the four T1, T2, T3 and T4 parameters to 9 and T5 to 22 (Dovesi et al. 2018). The diagonalization of the Hamiltonian matrix was performed at 30 independent *k* vectors in the reciprocal space (Monkhorst net; Monkhorst and Pack 1976) by setting the shrinking factor IS to 4 (Dovesi et al. 2018). Unit-cell parameters and fractional coordinates were optimized by analytical gradient methods, as implemented in CRYSTAL17 (Civalleri et al. 2001; Dovesi et al. 2018). Geometry optimization was considered converged when each component of the gradient (TOLDEG parameter in CRYSTAL17) was smaller than 0.00003 Hartree/Bohr and displacements (TOLDEX) were smaller than 0.00012 Bohr with respect to the previous step. Simulations of the Raman spectra of omphacite at the *static limit* have been performed at pressures ranging from 0 to 6 GPa (with step of 2 GPa from 0 to 4 GPa and then a step of 1 GPa from 4 to 6 GPa) by using the keyword EXTPRESS. The wavenumbers of all normal modes were calculated at the Γ point within the limit of the harmonic approximation, by diagonalizing a mass-weighted Hessian matrix, whose elements are the second derivatives of the full potential of the crystal with respect to the mass-weighted atomic displacements (Pascale et al. 2004). Furthermore, in order to directly compare the computational data with the experimental ones, we followed the procedure reported in Ghignone et al. (2023) for the estimate of EoS parameters at a temperature of 298 K.

Results

Crystal chemistry

The EMPA results for sample natural-8, annealed-3, and annealed-7 are reported in Table 1. Within uncertainties the compositions of all three specimens are the same as those reported by

Boffa Ballaran et al. (1998a). Sample natural-11 was unfortunately lost during the polishing procedure, so in the subsequent analyses we assumed that it has the same chemical composition of sample natural-8.

The structure of samples natural-8 and natural-11 is refined in *P*2/*n*, indicating chemical ordering, whereas samples annealed-3 and annealed-7 exhibit *C*2/*c* space symmetry typical of chemically disordered omphacites. The unit-cell parameters for all samples are given in Table 2, along with those calculated by HF/DFT simulations for fully ordered $Jd_{50}Di_{50}$ omphacite. The M1 site is commonly occupied by small cations such as Mg^{2+}, Al^{3+}, Fe^{3+} and Fe^{2+}, while larger cations such as Ca^{2+} and Na^{+} are at the M2 site. In the case of chemical order-disorder phenomena, the site occupancy factors are used to calculate the order parameters Q_{M1} and Q_{M2} (Carpenter et al. 1990a) as follows:

$$Q_{\mathrm{M1}} = \frac{\left|\frac{(\mathrm{Al}+\mathrm{Fe}^{3+})_{\mathrm{M1}} - (\mathrm{Al}+\mathrm{Fe}^{3+})_{\mathrm{M11}}}{(\mathrm{Al}+\mathrm{Fe}^{3+})_{\mathrm{M1}} + (\mathrm{Al}+\mathrm{Fe}^{3+})_{\mathrm{M11}}}\right| + \left|\frac{(\mathrm{Mg}+\mathrm{Fe}^{2+})_{\mathrm{M1}} - (\mathrm{Mg}+\mathrm{Fe}^{2+})_{\mathrm{M11}}}{(\mathrm{Mg}+\mathrm{Fe}^{2+})_{\mathrm{M1}} + (\mathrm{Mg}+\mathrm{Fe}^{2+})_{\mathrm{M11}}}\right|}{2}$$

$$Q_{\mathrm{M2}} = \frac{\left|\frac{\mathrm{Na}_{\mathrm{M2}} - \mathrm{Na}_{\mathrm{M21}}}{\mathrm{Na}_{\mathrm{M2}} + \mathrm{Na}_{\mathrm{M21}}}\right| + \left|\frac{\mathrm{Ca}_{\mathrm{M2}} - \mathrm{Ca}_{\mathrm{M21}}}{\mathrm{Ca}_{\mathrm{M2}} + \mathrm{Ca}_{\mathrm{M21}}}\right|}{2}$$

In natural samples the long-range order parameter at M1 is commonly twice larger than that at M2, i.e. $Q_{M1} \sim 2Q_{M2}$. (Boffa Ballaran et al. 1998a; Skelton and Walker 2015). The refined values of the site occupancy factors and subsequently calculated order parameters (see Table 3) are in a good agreement with those reported by Boffa Ballaran et al. (1998a). Sample natural-8 is slightly less ordered than natural-11 (Table 3). In Table S1 in the Online Materials the bond distances and the polyhedral volumes are reported.

Raman scattering at ambient conditions

According to group theory (e.g., Kroumova et al. 2003), at the Brillouin-zone centre there are Γ_{opt} = $14A_g$ + $13A_u$ + $16B_g$ + $14B_u$ optical phonon modes in chemically disordered omphacite

($C2/c$) and $\Gamma_{opt} = 28A_g + 27A_u + 32B_g + 30B_u$ in chemically ordered omphacite ($P2/n$). The A_u and B_u are infrared-active, while A_g and B_g modes are Raman-active. Only A_g modes should appear in parallel polarized Raman spectra measured when the pyroxene prism axis is parallel or perpendicular to the polarization of the incident light, as it was in our scattering geometry. Therefore, 28 peaks are expected in the Raman spectra of samples natural-8 and natural-11 and 14 peaks in the spectra of samples annealed-3 and annealed-7. Indeed 14 peaks were observed for chemically disordered omphacite (see Figure 2 and Table 4), but only 22 peaks were resolved for chemically ordered omphacite. This can be due to peak overlapping (e.g. the peaks near 1021 and 1029 cm^{-1}) or weak diagonal components (e.g. the peaks near 158, 281 and 452 cm^{-1}) of the Raman polarizability tensor, as indicated by the results of HF/DFT calculations. The calculated phonon wavenumbers of A_g modes in $P2/n$ at zero pressure match very well the observed Raman-peaks positions at atmospheric pressure (Table 4). The calculated and observed relative peak intensities in the parallel-polarized Raman spectra are also in a very good agreement (see Fig. 3a). A complete list of the Raman active phonon modes in fully ordered $Jd_{50}Di_{50}$ omphacite as well as the Raman polarizability tensors derived from HF/DFT calculations at P = 0 GPa and T = 0 K are given in the Online Materials (Table S2).

The assignment of each Raman peak to a definitive atomic vibration can be achieved by direct inspection of the calculated atomic vector displacements. The strongest experimentally observed Raman signals are then assigned as follows:

- The A_g modes in the range 950 and 1050 cm^{-1} are related to the Si-O_{nb} bond stretching (O_{nb} = non-bridging oxygen, which is not shared between two TO_4). Chemically disordered omphacite exhibits one peak observed near 1017 cm^{-1}, whereas ordered omphacite is characterized by the splitting of this peak into two components at about 1007 and 1029 cm^{-1}, due to the reduction of the translational symmetry.

- The strong peak at 688 cm^{-1}, typical of both chemically ordered and disordered omphacite, arises from A_g mode comprising Si–O_b–Si bond bending vibrations.

- The A_g modes at 375, 382, 402 and 411 cm^{-1} are related to $M1O_6$ and $M11O_6$ bending and TO_4 rotation around **c**.

- The A_g mode at 337 cm^{-1} in ordered omphacite is related to M1-cation vibrations parallel to the **b** axis and TO_4 rotation around the **c** axis. Note that the tilt angle is defined as the out-of-plane tilting of the basal face of the tetrahedra with respect to the plane (100) (Cameron et al. 1973).

- The A_g mode at 300 cm^{-1} in chemically ordered omphacite is due to M1-cation and ^{M2}Na vibrations parallel to **b**.

- The A_g mode at 271 cm^{-1} is associated with vibrations of M-site cations along **b** and TO_4 translation along **a**.

- The A_g mode at 215 cm^{-1} is mainly related to SiO_4 rotation around **a**.

Sketches of selected vibrational modes are presented in Figure S1 in the Online Materials.

It should be emphasized that the peak FWHM is affected by the ordering of the cations at the six- and eight-coordinated sites and it increases with cation disorder, as reported by Katerinopoulou et al. (2008).

Pressure dependence of Raman spectra

Figure 4 shows the pressure evolution of Raman spectra of chemically ordered omphacite. No change in the number of observed peaks occurs in the investigated pressure range. In accordance with theory, the strongest peak at 688 cm^{-1} gradually increases in wavenumber upon pressure increase, while its FWHM increases slightly, but within the spectral resolution (see Figure 5). The former is due to the pressure-induced decrease in the atomic distances and the

subsequent increase in the effective interatomic force constants, whereas the latter is related to the fact that the phonon decay and hence the peak FWHM should not change with pressure in the absence of structural transformations. Figure 5 also demonstrates that the phonon compressibility $\beta_\omega = \frac{1}{\omega_0}\frac{d\omega}{dP}$ of the A_g mode near 688 cm^{-1} does not depend on the chemical order, which makes this peak a potential candidate for wavenumber-pressure calibration. The linear fit $\omega(P) = \omega_0 + \frac{d\omega}{dP} P$ to the experimental data points gives ω_0 = 680.3(2), $\frac{d\omega}{dP}$ = 3.32(3), and $\beta_\omega = 0.00488(5)$ GPa^{-1}. Then using the relation $P = \frac{\omega - 680.3}{3.32}$, the pressure can be determined with an accuracy of ~0.1 GPa. Further experiments can improve the statistics of $\omega(P)$ data points, which in turn will reduce the errors in the coefficients of polynomial fit and consequently, will reduce the propagating uncertainties in P_{inc}, that is the residual pressure.

A few Raman peaks for chemically ordered omphacite show anomalous behavior near 4.5-5 GPa: (i) the pressure dependence of the average wavenumber of the two components related to the Si-O_{nb} bond stretching shows a discontinuity near 5 GPa (Figure 6a), although the $\frac{d\omega}{dP}$ value remains nearly the same above 5 GPa; (ii) the slope of $\omega(P)$ of the peaks near 375 cm^{-1} and 337 cm^{-1}, both arising from $M1O_6$ vibrations and SiO_4 rotations, changes around 4.5 GPa (Figure 6b and c) and above this pressure the corresponding phonon compressibility equals to that of disordered omphacite; (iii) the FWHM of the peak near 271 cm^{-1}, generated by M-cation vibrations and SiO_4 translations, becomes smaller above 5 GPa (Figure 6d).

In order to simulate the pressure dependence of the phonon modes, unit-cell parameters (reported in Table 2) and fractional coordinates were optimized by analytical gradient methods and the equation of state (EoS) at room temperature was modelled. As can be seen in Table 5, the calculated EoS parameters are in good agreement with previously published experimental results (Pavese et al. 2001; Pandolfo et al. 2012b; Zhang et al. 2016).

The pressure dependence of the phonon wavenumbers of fully ordered omphacites was simulated in the pressure range 0-11 GPa, while the Raman intensities were calculated at 0, 2, 4, 5 and 6 GPa. The correspondence between experimental and calculated spectra at high pressure is very good (Figure 3b). The calculated $\frac{d\omega}{dP}$ of the main peaks also match very well the corresponding experimentally observed $\omega(P)$ slopes (see Figure 7).

Discussions

The hybrid HF/DFT simulations reveal that the anomalous $\omega(P)$ behavior of the peak ~337 cm^{-1} for chemically ordered omphacite can be explained by enhanced phonon-phonon interactions near 4.7 GPa. The ab initio simulations reveal that in this spectral range there are actually two A_g modes, at 337 and 349 cm^{-1}. Having the same symmetry and similar energies, these A_g modes can interact and exchange intensity via the so-called *avoided intersection*, also referred to as energy-level anticrossing (Dresselhaus et al. 2008); that is, two modes of the same symmetry approach one another in energy but without energy crossing. Indeed, the wavenumbers of the two A_g modes become very close to each other at a volume of about 413 $Å^3$ (see the insert in Figure 7), corresponding to a pressure of 4.7 GPa, while at higher pressure they diverge. These two Raman peaks could be experimentally distinguished for sample natural-8 when measured in air, but not under high pressure in DAC, so that only one peak at about 337 cm^{-1} was used in the fitting model for high-pressure spectra. However, as can be seen in Figure 7, the experimental and simulated pressure trend for the A_g mode near 337 cm^{-1} are in a very good agreement.

It should be emphasized that above the pressure of A_g-phonon anticrossing, the phonon compressibility of the mode near 337 cm^{-1} in chemically ordered omphacite becomes the same as that in chemically disordered omphacite. The same is valid for the A_g mode near 375 cm^{-1}. Both phonon modes involve SiO_4 tilting and M-cation vibrations and the change in β_ω should be related

to a change in the M-O-Si interactions. External pressure alone cannot mobilize M-site cations to form a chemically disordered state above 4.5 GPa. However, pressure can trigger a redistribution of the local elastic strains related to the difference in the ionic sizes of the M-site cations, leading to unified MO_6 volumes and consequently, averaged effective M-O-Si force constants that appear to be the same as a state of site-occupancy disorder. In addition, both the zenithal and azimuthal components of the out-of-plane basal tilts of tetrahedra, which change as a function of the degree of order (for exact definitions see Boffa Ballaran et al. 1998a and Cámara et al. 1998), may also change as a consequence of compression, related also to the unified volume compressibility of the M1 and M11 octahedra. Chemical disorder is difficult to implement in ab initio simulations. However, based on the combined experimental and HF/DFT results presented here, we speculate that the pressure-enhanced phonon-phonon interactions near 4.5-5 GPa trigger the homogenization of local elastic strains associated with chemical order at the (M1, M11) and (M2, M21) sites, respectively. This phenomenon should be responsible also for the anomaly in the averaged $\omega(P)$ of the Si-O_{nb} bond stretching mode observed near 1017 cm^{-1}, because M-O interactions have a secondary effect on the energy of this phonon mode. The experimentally observed reduction of the FWHM of the 271-cm^{-1} peak, resulting primarily from M-cation vibrations, is also consistent with the assumption for a smaller dispersion in the MO_6 size above ~4.5 GPa.

For ordered omphacite a slight anomaly in the pressure dependence of the $M1,11O_6$ volumes has been reported at about 4 GPa by Pandolfo et al. (2012b), which was attributed to a pressure-induced change of the tilt angle for both $T1O_4$ and $T2O_4$ tetrahedra. This observation corroborates with the anomalies reported here for the phonon modes at about 1017, 375, 337, and 271 cm^{-1}. Moreover, we show that the position of the well resolved Raman peak at 688 cm^{-1}, generated by Si-O_{br}-Si bond bending A_g mode, exhibits a strong pressure dependence, which is not

affected by the presence or absence of chemical order. That is, the temperature-induced change of the translational symmetry due to site-occupancy order-disorder processes does not influence the wavenumber of the Si-O_{br}-Si bond bending and therefore, this phonon mode properly reflects the strained state of an omphacite inclusion associated with the metamorphic conditions. Besides, HF/DFT calculations indicate that this mode exhibits the strongest polycrystalline isotropic Raman intensity (see Table 4), ensuring that the peak near 688 cm^{-1} can be experimentally detected in any random orientation of an omphacite inclusion. Thus, as garnets do not show Raman scattering in this spectral range (Kolesov and Geiger 1998), this peak seems to be a promising candidate to be used for estimating the residual pressure for omphacite-in-garnet inclusion-host systems. On the other hand, the FWHM of this peak does not change with pressure, but it is indicative of the absence or presence of chemical cation order. When an instrumental resolution of 2 cm^{-1} is used, disordered omphacite shows a FWHM for the 688-cm^{-1}-peak around 16 cm^{-1}, whereas for omphacite with $Q_{M1} \cong 2Q_{M2} \cong 0.8$ the peak FWHM is around 12 cm^{-1}. A cation order parameter $Q_{M1} \cong 0.83$ corresponds to a closure temperature of about 600 K (Carpenter et al. 1990a). Therefore, a FWHM above 12 cm^{-1} implies that the omphacite inclusion has been trapped at T > 600 K. However, the Raman spectrum of omphacite and in particular the position of the wavenumber of the Si-O-Si bond bending mode depends on the chemical composition (Wang et al. 2001; Prencipe et al. 2012). Hence, further comprehensive studies on the compositional effect on the phonon compressibility for omphacites with diverse chemistry is required before utilizing omphacite-in-garnet systems for Raman elastic geothermobarometry applications.

Implications

Conventional thermobarometry techniques are commonly used in geological sciences for determining pressure and temperature conditions of mineral formation. These methods rely on

mineral assemblages and chemical compositions, providing valuable insights into metamorphic processes, but they are limited by assumptions of chemical thermodynamic equilibrium under hydrostatic pressure (Powell and Holland 2008; Gilio et al. 2022). On the other hand, Raman elastic thermobarometry provides a non-destructive in situ approach for estimating pressure and temperature conditions based on the elastic properties of an inclusion and its host. This technique, which is mostly independent of chemical equilibration, holds great promise for providing accurate thermobarometric data, but it is restricted to a few host-inclusion systems. The lack of calibrations of Raman shifts with pressure, as well as of elastic properties at variable pressure and temperature, requires further experiments to improve and validate this method in geological studies (Kohn et al. 2023).

The present study represents the first step towards enabling the use of omphacite inclusions for elastic geothermobarometry purposes using Raman spectroscopy. We demonstrate that knowing the EoS and the composition of the inclusion, determined by EMPA analysis, it will be possible to a first approximation to estimate its residual pressure using Raman spectroscopy. For this purpose, one should comprehensively study the effect of the relevant thermodynamic variables on the phonon wavenumbers, namely elastic stress (or hydrostatic pressure), chemical composition, degree of chemical order. That is, one should: (i) establish relationships between phonon wavenumber and external elastic stresses/hydrostatic pressure, i.e. $\omega(P)$; (ii) a robust relationship between the chemical composition, denoted here for simplicity with $\{x\}$, and the phonon wavenumber, i.e. $\omega(\{x\})$, (iii) the effect of chemical composition on phonon compressibilities, i.e. $\beta_\omega(\{x\})$; and (iv), the effect of chemical order on ω and β_ω. At the current stage, this can only be done using empirical calibrations such as $\omega(P) = \omega_0+(d\omega/dP)P$ for selected phonon modes, which have been proved to be insensitive to the degree of chemical order, so that at least one parameter influencing the phonon frequencies can be eliminated. Further ab initio

calculations will enable, at least for the ordered structure, to calculate the Grüneisen tensor for a correct estimate of the residual strains (see Murri et al. 2018 for further details). The subsequent key point to enable the use of omphacite for elastic geobarometric purposes is the contrast in their elastic properties with respect to those of the host. Garnet is a significantly stiffer material compared to omphacite. Synthetic $Prp_{60}Alm_{40}$ garnet has a bulk modulus (K_{T0}) of 167.2 (17) GPa (Milani et al. 2015); on the other hand, omphacite has a lower K_{T0}, ranging from 122(1) to 119(2) GPa (Pandolfo et al. 2012a, b), thus implying a larger relaxation of omphacite volume than its host garnet and the building up of a significant remanent inclusion pressure from which it is possible to calculate the entrapment conditions (Korsakov et al. 2009). Furthermore, omphacite has a softer bulk modulus compared to zircon, but it is stiffer than quartz. The combination of their thermoelastic properties contributes to the isomekes trends: the isomekes of omphacite resemble those of quartz, making it a potential barometer.

To the aim of recalculating the entrapment conditions, knowing the elastic behavior as a function of composition and ordering state becomes crucial. Previous high-pressure single-crystal XRD analyses on omphacite from the same location as that of omphacite used in our study revealed K_{T0} = 122(1) GPa and K' = 5.1(3) for ordered omphacite, and K_{T0} = 119(2) GPa and K' = 5.7(6) for the disordered omphacite (Pandolfo et al. 2012a, b), i.e. within the uncertainties ordered and disordered omphacite exhibit a very similar volume compressibility up to 7.5 GPa (Table 5). Regarding the composition, Pandolfo et al. (2012a) discussed the bulk modulus dependence on the composition in terms of jadeite and diopside solid solution and proposed the following equation:

$$K_{T0} = 106(1)GPa + 0.28(2) \times Jd_{(mol\%)}$$

Our preliminary results based on the calculated EoS of omphacite indicate that the slope of omphacite-in-garnet isomeke is close to the slope of quartz-in-garnet isomeke (Figure 8) which

makes omphacite a good candidate for elastic geobarometry. Here we present an example of garnet host with omphacite inclusions because it is a widespread host-inclusion system in several geological settings. For example, omphacite in garnet could be extremely useful in low-silica systems like metabasites (the most widespread lithotype of eclogites) where quartz is not stable and omphacite becomes a suitable common phase for retrieving metamorphic peak conditions. Furthermore, omphacite-in-garnet host-inclusion system will provide fundamental hints for low-pressure and high-temperature geological settings where both quartz and zircon inclusions in garnet have considerable shortcomings. The first comes from the high temperature α-quartz $\leftrightarrow$ β-quartz phase transition and related effects on the atomic dynamics (e.g., Murri et al. 2019a) and the latter because of the high-temperature elastic reset in zircon (Campomenosi et al. 2022).

While the slope of the isomekes and the different character of the phase transition provides significant advantages for omphacite-in-garnet with respect to quartz- and zircon-in-garnet because it extends significantly the PT space of potential applicability, however the large spacing between the isomekes, far greater than that of quartz and zircon, may be a significant shortcoming. Because of the large spacing, omphacite inclusions in garnet will require higher precision in determining P_{inc} from Raman spectroscopy.

In this paper we show that below ~4.5 GPa the phonon compressibility of MO_6 octahedra is larger for the chemically ordered omphacite than for its disordered counterpart, whereas above 4.5 GPa the elastic behavior is unified, probably because the external pressure leads to homogeneous distribution of the internal chemically-induced local stresses. The strong Raman peak near 688 cm^{-1}, arising from Si-O_{br}-Si bond bending, seems to be a promising Raman marker for residual pressure via its position, and indicative of closure temperature via its width. However, further comprehensive analysis of the effect of composition and the cation order degree on all

451 omphacite Raman-active modes and their pressure behavior is required to develop a protocol for
452 the proper utilization of omphacite-in-garnet systems in Raman elastic geothermobarometry.
453

454 **Acknowledgements**

455 This work was funded by the Italian Ministry of University and Research (MIUR) through a
456 PhD grant to L. Baratelli and to F. Cámara and L. Baratelli through the project "Dipartimenti di
457 Eccellenza 2023–2027", and by European Research Council under the European Union's Horizon
458 2020 research and innovation program grant agreement 714936 (ERC-STG TRUE DEPTHS) to M.
459 Alvaro. M. Murri is supported by an A. von Humboldt research fellowship. This work has also been
460 partly supported by the PRIN-MUR project "THALES" Prot.2020WPMFE9_003. M. Alvaro is also
461 supported by the Highlight funded by Fondi Regione Lombardia DGR 3776.
462

References cited

Alvaro, M., Domeneghetti, M.C., Fioretti, A.M., Cámara, F., and Marinangeli, L. (2015). A new calibration to determine the closure temperatures of Fe-Mg ordering in augite from nakhlites. Meteoritics & Planetary Science, 50(3), 499–507.

Andò, S., and Garzanti, E. (2014) Raman spectroscopy in heavy-mineral studies. Geological Society, London, Special Publications, 386(1), 395–412.

Angel, R.J., Bujak, M., Zhao, J., Gatta, G.D., and Jacobsen, S.D. (2007) Effective hydrostatic limits of pressure media for high-pressure crystallographic studies. Journal of Applied Crystallography, 40(1), 26–32.

Angel, R.J., Alvaro, M., Miletich, R., and Nestola, F. (2017a) A simple and generalised P-T-V EoS for continuous phase transitions, implemented in EosFit and applied to quartz. Contributions to Mineralogy and Petrology, 172(5), 29.

Angel, R.J., Mazzucchelli, M.L., Alvaro, M., and Nestola, F. (2017b). EosFit-Pinc: A simple GUI for host-inclusion elastic thermobarometry. American Mineralogist, 102(9), 1957–1960.

Angel, R.J., Gilio, M., Mazzucchelli, M., and Alvaro, M. (2022) Garnet EoS: a critical review and synthesis. Contributions to Mineralogy and Petrology, 177(54).

Anzolini, C., Prencipe, M., Alvaro, M., Romano, C., Vona, A., Lorenzon, S., Smith, E.M., Brenker, F.E. and Nestola, F. (2018) Depth of formation of super-deep diamonds: Raman barometry of $CaSiO_3$-walstromite inclusions. American Mineralogist, 103(1), 69–74.

Beata G, Perego G, Civalleri B (2019) CRYSPLOT: A new tool to visualize physical and chemical properties of molecules, polymers, surfaces, and crystalline solids. Journal of Computational Chemistry, 40:2329-2338.

485 Boffa Ballaran, T., Carpenter, M.A., Domeneghetti, M.C., and Tazzoli, V. (1998a) Structural
486 mechanisms of solid solution and cation ordering in augite-jadeite pyroxenes: I. A macroscopic
487 perspective. American Mineralogist, 83, 419–433.
488 Boffa Ballaran, T., Carpenter, M.A., Domeneghetti, M.C., Salje, E.K.H., and Tazzoli, V. (1998b)
489 Structural mechanisms of solid solution and cation ordering in augite-jadeite pyroxenes: II. A
490 microscopic perspective. American Mineralogist, 83, 434–443.
491 Buzatu, A., and Buzgar, N. (2010) The Raman study of single-chain silicates. Analele Ştiinţifice ale
492 Universităţii “AI. I. Cuza” din Iaşi, Geologie, 56(1), 107–125.
493 Cámara, F., Nieto, F., and Oberti, R. (1998) Effects of Fe^{2+} and Fe^{3+} contents on cation ordering in
494 omphacite. European Journal of Mineralogy, 10, 889–996.
495 Cameron, M., Sueno, S., Prewitt, C.T., and Papike, J.J. (1973) High temperature crystal chemistry of
496 acmite, diopside, hedenbergite, jadeite, spodumene, and ureyite. American Mineralogist, 58, 594–
497 618.
498 Campomenosi, N., Scambelluri, M., Angel, R.J., Hermann, J., Mazzucchelli, M.L., Mihailova, B.,
499 Piccoli, F., and Alvaro, M. (2021) Using the elastic properties of zircon-garnet host-inclusion pairs
500 for thermobarometry of the ultrahigh-pressure Dora-Maira whiteschists: problems and
501 perspectives. Contributions to Mineralogy and Petrology, 176(36).
502 Campomenosi, N., Angel, R.J., Alvaro, M., and Mihailova, B. (2022) Resetting of zircon inclusions in
503 garnet: Implications for elastic thermobarometry. Geology, 51(1), 23–27.
504 Carli, C., Barbaro, A., Murri, M., Domeneghetti, C.M., Langone, A., Bruschini, E., Stephant, A.,
505 Alvaro, M., Stefani, S., Cuppone, T., Casalini, M., Migliorini, A., Roush, T., and Pratesi, G. (2023) Al
506 Huwaysah 010: the most reduced brachinite, so far. Meteoritics & Planetary Science, 58(6), 855–
507 874.

Carpenter, M.A. (1980) Mechanisms of exsolution in sodic pyroxenes. Contributions to Mineralogy and Petrology, 71, 289–300.

Carpenter, M.A. (1981a) Time-Temperature-Transformation (TTT) analysis of cation disordering in omphacite. Contributions to Mineralogy and Petrology, 78, 433–440.

Carpenter, M.A. (1981b) Omphacite microstructures as time-temperature indicators of blueschist and eclogite facies metamorphism. Contributions to Mineralogy and Petrology, 78, 441–451.

Carpenter, M.A., Domeneghetti, M.C., and Tazzoli, V. (1990a) Application of Landau theory to cation ordering in omphacite I: Equilibrium behaviour. European Journal of Mineralogy, 2(1), 7–18.

Carpenter, M.A., Domeneghetti, M.C., and Tazzoli, V. (1990b) Application of Landau theory to cation ordering in omphacite II: Kinetic behaviour. European Journal of Mineralogy, 2(1), 19–28.

Civalleri, B., D'Arco, P., Orlando, R., Saunders, V., and Dovesi, R. (2001) Hartree-Fock geometry optimisation of periodic systems with the CRYSTAL code. Chemical Physics Letters, 348, 131–138.

Dovesi, R., Erba, A., Orlando, R., Zicovich-Wilson, C.M., Civalleri, B., Maschio, L., R´erat, M., Casassa, S., Baima, J., Salustro, S., and Kirtman, B. (2018) Quantum-Mechanical Condensed Matter Simulations with CRYSTAL. WIREs Computational Molecular Science, e1360.

Dresselhaus, M.S., Dresselhaus, G., and Jorio, A. (2008) Group theory: application to the physics of condensed matter, 582 p. Springer-Verlag, Berlin.

Ehlers, A.M., Zaffiro, G., Angel, R.J., Boffa-Ballaran, T., Carpenter, M.A., Alvaro, M., and Ross, N.L. (2022) Thermoelastic properties of zircon: Implications for geothermobarometry. American Mineralogist, 107(1), 74–81.

Franz, L., Sun, T.T., Hänni, H.A., De Capitani, C., Thanasuthipitak, T., and Atichat, W. (2014) A comparative study of jadeite, omphacite and kosmochlor jades from Myanmar, and suggestions for a practical nomenclature. The Journal of Gemmology, 34(3), 210–229.

Ghignone, S., Prencipe, M., Manzotti, P., Bruno, M., Boero, F., Borghini, A., Costa, E., Ciriotti, M., Scaramuzzo, E. (2023) The Raman spectrum of florencite-(REE) [$REEAl_3(PO_4)_2(OH)_6$]: An integrated experimental and computational approach. Journal of Raman Spectroscopy, 1.

Gianola, O., Costa, B., Ferri, F., Gilio, M., Petrelli, M., Murri, M., Barbaro, A., Alvaro, M., Rodríguez-Vargas, A., Poli, S., and Cesare, B. (2023). Melt inclusions in arclogitic xenoliths constrain the genesis of the lower continental arc crust beneath the Northern Volcanic Zone, Colombia. Journal of Petrology, 64(6), egad038.

Gilio, M., Scambelluri, M., Agostini, S., Godard, M., Pettke, T., Agar, P., Locatelli, M., and Angiboust, S. (2020) Fingerprinting and relocating tectonic slices along the plate interface: Evidence from the Lago Superiore unit at Monviso (Western Alps). Lithos, 352-353, 105308.

Gilio, M., Angel, R.J., Alvaro, M. (2021) Elastic geobarometry: How to work with residual inclusion strains and pressures. American Mineralogist, 106(9), 1530–1533.

Gilio, M., Scambelluri, M., Angel, R.J., Alvaro, M. (2022) The contribution of elastic geothermobarometry to the debate on HP versus UHP metamorphism. Journal of Metamorphic Geology, 40(2), 229–242.

Hawthorne, F.C., Ungaretti, L., and Oberti, R. (1995) Site populations in minerals: terminology and presentation of results of crystal-structure refinement. The Canadian Mineralogist, 33, 907–911.

Katerinopoulou, A., Musso, M., and Amthauer, G. (2008) A Raman spectroscopic study of the phase transition in omphacite. Vibrational Spectroscopy, 48, 163–167.

Kohn, M.J., Mazzucchelli, M.L., Alvaro, M. (2023) Elastic Thermobarometry. Annual Review of Earth and Planetary Sciences, 51, 331–366.

Kolesov, B.A., and Geiger, C.A. (1998) Raman scattering in silicate garnets: an investigation of their resonance intensities. Journal of Raman Spectroscopy, 28, 659–662.

Korsakov, A.V., Perraki, M., Zhukov, V.P., De Gussem, K., Vandenabeele, P., and Tomilenko, A.A. (2009) Is quartz a potential indicator of ultrahigh-pressure metamorphism? Laser Raman spectroscopy of quartz inclusions in ultrahigh-pressure garnets. European Journal of Mineralogy, 21, 1313–1323.

Kroumova, E., Aroyo, M., Mato, J.P., Kirov, A., Capillas, C., Ivantchev, S., and Wondratschek, H. (2003) Bilbao crystallographic server: useful databases and tools for phase-transition studies. Phase Transitions, 76, 155–170.

Lee, C., Yang, W., and Parr, R.G. (1988) Development of the Colle-Salvetti correlation-energy formula into a functional of the electron density. Physical Review B, 37, 785–789.

Lentz, R.C.F., McCoy, T.J., Collins, L.E., Corrigan, C.M., Benedix, G.K., Taylor, G.J., and Harvey, R.P. (2011). Theo's Flow, Ontario, Canada: A terrestrial analog for the Martian nakhlite meteorites. Geological Society of America Special Papers, 483, 263–277.

Matthes, S., and Schmidt, K. (1974) Eclogites of the Münchberg Mass, NE Bavaria. Fortschritte der Mineralogie, 52, 33–57.

McCormick, T.C. (1986) Crystal-chemical aspects of nonstoichiometric pyroxenes. American Mineralogist, 71, 1434–1440.

Meyer, H.O.A., and Boyd, F.R. (1972) Composition and origin of crystalline inclusions in natural diamonds. Geochimica et Cosmochimica Acta, 86, 1255–1273.

Mihailova, B., Waeselmann, N., Stangarone, C., Angel, R.J., Prencipe, M., and Alvaro, M. (2019) The pressure-induced phase transition(s) of $ZrSiO_4$: revised. Physics and Chemistry of Minerals, 46, 807–814.

Momma, K., and Izumi, F. (2008) Vesta: a three-dimensional visualization system for electronic and structural analysis. Journal of Applied Crystallography, 41, 653–658.

Monkhorst, H.J., and Pack, J.D. (1976) Special points for Brillouin-zone integrations. Physical Review B, 12, 5188–5193.

Morimoto, N. (1988) Nomenclature of Pyroxenes. Mineralogical Magazine, 52, 535–550.

Munro, R., Piermarini, J., Block, S., and Holzapfel, W. (1985) Model line-shape analysis for the ruby R lines used for pressure measurements. Journal of Applied Physics, 57, 165–169.

Murri, M., Scandolo, L., Fioretti, A.M., Nestola, F., Domeneghetti, C.M., and Alvaro, M. (2016). The role of Fe content on the Fe-Mg exchange reaction in augite. American Mineralogist, 101(12), 2747–2750.

Murri, M., Mazzucchelli, M.L., Campomenosi, N., Korsakov, A.V., Prencipe, M., Mihailova, B.D., Scambelluri, M., Angel, R.J., and Alvaro, M. (2018) Raman elastic geobarometry for anisotropic mineral inclusions. American Mineralogist, 103, 1869–1872.

Murri, M., Alvaro, M., Angel, R.J., Prencipe, M., and Mihailova, B.D. (2019a) The effects of non-hydrostatic stress on the structure and properties of alpha-quartz. Physics and Chemistry of Minerals, 46, 487–499.

Murri, M., Domeneghetti, M.C., Fioretti, A.M., Nestola, F., Vetere, F., Perugini, D., Pisello, A., Faccenda, M., and Alvaro, M. (2019b). Cooling history and emplacement of a pyroxenitic lava as proxy for understanding Martian lava flows. Scientific Reports, 9(1), 1–7.

Nestola, F., Alvaro, M., Casati, M.N., Wilhelm, H., Kleppe, A.K., Jephcoat, A.P., Domeneghetti, M.C., and Harris, J.W. (2016) Source assemblage types for cratonic diamonds from X-ray synchrotron diffraction. Lithos, 265, 334–338.

Nestola, F., Prencipe, M., Nimis, P., Sgreva, N., Perritt, S.H., Chinn, I.L. and Zaffiro, G. (2018) Toward a robust elastic geobarometry of kyanite inclusions in eclogitic diamonds. Journal of Geophysical Research: Solid Earth, 123, 6411–6423.

O'Brien, P.J. (1993). Partially retrograded eclogites of the Münchberg Massif, Germany: records of a multi-stage Variscan uplift history in the Bohemian Massif. Journal of Metamorphic Geology, 11, 241–260.

Pandolfo, F., Nestola, F., Cámara, F., and Domeneghetti, M.C. (2012a) New thermoelastic parameters of natural *C*2/*c* omphacite. Physics and Chemistry of Minerals, 39, 295–304.

Pandolfo, F., Nestola, F., Cámara, F., and Domeneghetti, M.C. (2012b) High-pressure behavior of space group *P*2/*n* omphacite. American Mineralogist, 97, 407–414.

Papike, J.J. (1980) Pyroxene mineralogy of the moon and meteorites. Mineralogical Society of America, Reviews in Mineralogy, Pyroxenes, 7, 495–525.

Pascale, F., Zicovich-Wilson, C.M., Lopez Gejo, F., Civalleri, B., Orlando, R., and Dovesi, R. (2004) The calculation of the vibrational frequencies of crystalline compounds and its implementation in the CRYSTAL code. Journal of Computational Chemistry, 25, 888–897.

Pasqualetto, L., Nestola, F., Jacob, D.E., Pamato, M.G., Oliveira, B., Perritt, S., Chinn, I., Nimis, P., Milani, S., and Harris, J.W. (2022) Protogenetic clinopyroxene inclusions in diamond and Nd diffusion modeling—Implications for diamond dating. Geology, 50(9), 1038–1042.

Pavese, A., Bocchio, R., and Ivaldi, G. (2000) In situ high temperature single crystal X-ray diffraction study of a natural omphacite. Mineralogical Magazine, 64(6), 983–993.

Pavese, A., Diella, V., Devy, D., and Hanfland, M. (2001) Synchrotron X-ray diffraction study of a natural P2/n omphacites at high pressure conditions. Physics and Chemistry of Minerals, 28, 9–16.

Phakey, P.P., and Ghose, S. (1973) Direct observation of Anti-Phase Domain structure in omphacite. Contributions to Mineralogy and Petrology, 39, 239–245.

Philpotts, A., and Ague, J. (2009) Principles of igneous and metamorphic petrology, 667 p. Cambridge University Press, Second Edition.

Pouchou, J.L., and Pichoir, F. (1985) 'PAP' Φ(ρZ) procedure for improved quantitative microanalysis. In J.T. Armstrong Ed., Microbeam Analysis, p. 104–106. San Francisco Press.

Powell, R., and Holland, T.J.B. (2008) On thermobarometry. Journal of Metamorphic Geology, 26(2), 155–179.

Prencipe, M. (2012) Simulation of vibrational spectra of crystals by ab initio calculations: an invaluable aid in the assignment and interpretation of the Raman signals. The case of jadeite ($NaAlSi_2O_6$). Journal of Raman Spectroscopy, 43, 1567–1569.

Prencipe, M. (2018) Quantum mechanics in Earth sciences: a one-century-old story. Rendiconti Lincei. Scienze Fisiche e Naturali, 30, 239–259.

Prencipe, M., Scanavino, I., Nestola, F., Merlini, M., Civalleri, B., Bruno, M., and Dovesi, R. (2011) High-pressure thermo-elastic properties of beryl ($Al_4Be_6Si_{12}O_{36}$) from ab initio calculations, and observations about the source of thermal expansion. Physics and Chemistry of Minerals, 38, 223–239.

Prencipe, M., Mantovani, L., Tribaudino, M., Bersani, D., and Lottici, P.P. (2012) The Raman spectrum of diopside: a comparison between ab initio calculated and experimentally measured frequencies. European Journal of Mineralogy, 3, 457–464.

Robinson, K., Gibbs, G.V., and Ribbe, P.H. (1971) Quadratic elongation: a quantitative measure of distortion in coordination polyhedra. Science, 172, 567–570.

Sheldrick, G.M. (2015) Crystal structure refinement with SHELX. Acta Crystallographica, C71, 3–8.

Skelton, R., and Walker, A.M. (2015) The effect of cation order on the elasticity of omphacite from atomistic calculations. Physics and Chemistry of Minerals, 42, 677–691.

Sophia, G., Baranek, P., Sarrazin, C., Rérat, M., and Dovesi, R. (2014) Systematic influence of atomic substitution on the phase diagram of ABO_3 ferroelectric perovskites. (Online) Available: https://www.crystal.unito.it/Basis_Sets/tin.html

Stangarone, C., Tribaudino, M., Prencipe, M., and Lottici, P.P. (2016) Raman modes in *Pbca* enstatite ($Mg_2Si_2O_6$): an assignment by quantum mechanical calculation to interpret experimental results. Journal of Raman Spectroscopy, 47, 1247–1258.

Valenzano, L., Torres, F.J., Doll, K., Pascale, F., Zicovich-Wilson, C.M., and Dovesi, R. (2006) Ab initio study of the vibrational spectrum and related properties of crystalline compounds; the case of $CaCO_3$ calcite. Zeitschrift für Physikalische Chemie, 220, 893–912.

Van Roermund, H.L.M., and Lardeaux, J.M. (1991) Modification of antiphase domain sizes in omphacite by dislocation glide and creep mechanisms and its petrological consequences. Mineralogical Magazine, 55, 397–407.

Wang, A., Jolliff, B.L., Haskin, L.A., Kuebler, K.E., and Viskupic, K.M. (2001). Characterization and comparison of structural and compositional features of planetary quadrilateral pyroxenes by Raman spectroscopy. American Mineralogist, 86(7-8), 790–806.

Wilson, A.J.C. (1995) International Tables for Crystallography. Volume C. Kluwer Academic Publishers, Dordrecht.

Wu, Z., and Cohen, R.E. (2006) More accurate generalized gradient approximation for solids. Physical Review B, 73, 235116.

Zhang, D., Hu, Y., and Dera, P.K. (2016) Compressional behavior of omphacite to 47 GPa. Physics and Chemistry of Minerals, 43, 707–715.

Zhong, X., Andersen, N.H., Dabrowski, M., and Jamtveit, B. (2019) Zircon and quartz inclusions in garnet used for complementary Raman thermobarometry: application to the Holsnøy eclogite, Bergen Arcs, Western Norway. Contributions to Mineralogy and Petrology, 174(50).

668 **Captions**

669 **Table 1.** Electron microprobe analyses in oxide wt% and chemical formulae in atoms per formula
670 unit, based on six oxygen atoms

671 **Table 2.** Unit-cell parameters of the analyzed crystals, compared to the ab initio calculated ones

672 **Table 3.** Site occupancy factors, order parameters and mean bond distances (given in Å) refined
673 from single-crystal XRD data with chemical constraints

674 **Table 4.** Calculated and experimental wavenumbers (ω, in cm^{-1}) of the A_g modes and relative
675 intensities normalized to 688 cm^{-1} mode (I, in arbitrary units) of omphacite

676 **Table 5.** Bulk modulus K_0, its pressure derivative K', the zero-pressure volume V_0 as well as the
677 order parameters Q_{M1} and Q_{M2}, pressure (P) and temperature (T) conditions of each study. The
678 EoSs were determined using single-crystal XRD for all experimental studies except for Pavese et al.
679 (2001), who used powder XRD

680 **Figure 1.** A structural fragment of ordered omphacite (space group symmetry $P2/n$). SiO_4
681 tetrahedra are shown in dark blue, M1 sites in orange, M11 sites in yellow, M2 in blue, and M21 in
682 light blue. The structure was prepared using the VESTA software package (Momma and Izumi
683 2008).

684 **Figure 2.** Raman spectra of chemically ordered (red and grey lines) and chemically disordered
685 (blue and green lines) omphacite, collected in (**c**||$\mathbf{E}_i$||$\mathbf{E}_s$) (samples natural-8 and annealed-3) or (**c**
686 $\perp$ $\mathbf{E}_i$ || $\mathbf{E}_s$) (samples natural-11 and annealed-7) scattering geometry at room temperature and
687 atmospheric pressure. The signals marked by * are not related to omphacite Raman-active phonon
688 modes.

689 **Figure 3.** Experimental and calculated Raman spectra of ordered omphacite ($P2/n$), at ~0 GPa (a)
690 and at ~5 GPa (b).

691 **Figure 4.** Pressure evolution of (**c**||$\mathbf{E}_i$||$\mathbf{E}_s$) Raman spectra of chemically ordered omphacite
692 (sample natural-11).

693 **Figure 5.** Pressure dependence of the wavenumber and FWHM of the strongest Raman peak at
694 688 cm^{-1}. Filled symbols are related to the ordered omphacites, while open symbols to the
695 disordered omphacites.

696 **Figure 6.** Pressure dependence of the wavenumber or FWHM of the peaks that show an anomaly
697 at about 5 GPa in ordered omphacite, along with the corresponding trends for disordered
698 omphacites: the average wavenumber of the two peaks near to 1007 and 1029 cm^{-1} (a); the slope
699 of the peaks at about 375 cm^{-1} (b) and 337 cm^{-1} (c) changes around 4.5 GPa; the FWHM of the
700 peak near 271 cm^{-1} becomes smaller above 5 GPa (d).

701 **Figure 7.** Experimental and calculated pressure dependence of the wavenumber of the A_g^{337} mode.
702 The slopes of the curves and the pressure at which they change are reported. The insert shows the
703 calculated wavenumbers of the two A_g modes that are involved in the anticrossing.

704 **Figure 8.** Calculated isomekes for quartz, zircon and omphacite inclusion in an almandine host,
705 obtained from the P_{inc} (equal to 0.0, 0.2, and 0.4 GPa) with the EoSFit–Pinc software (Angel et al.
706 2017b), using the equation of state of quartz (Angel et al. 2017a), zircon (Ehlers et al. 2022) and
707 almandine (Angel et al. 2022), while the HF/DFT calculated EoS was used for omphacite ($Jd_{50}Di_{50}$).
708 The α-β transition of quartz is represented in a red dashed line, line and the shaded vertical strip
709 represents the *P*2/*n*-to-*C*2/*c* omphacite transition.

710

This is the peer-reviewed, final accepted version for American Mineralogist, published by the Mineralogical Society of America.
The published version is subject to change. Cite as Authors (Year) Title. American Mineralogist, in press.
DOI: https://doi.org/10.2138/am-2023-9140. http://www.minsocam.org/

711 **Table 1**

	Natural-8 (10 pt)	Annealed-3 (5 pt)	Annealed-7 (3 pt)
SiO_2	56.31(26)	55.79(25)	54.83(45)
Al_2O_3	11.30(10)	11.24(6)	11.09(3)
TiO_2	0.12(4)	0.14(3)	0.12(2)
Cr_2O_3	0.04(4)	0.04(3)	0.29(1)
FeO	2.56(6)	2.57(10)	2.41(7)
MnO	0.01(2)	0.01(2)	0.02(3)
MgO	9.87(11)	9.84(11)	9.46(12)
CaO	15.27(11)	15.27(6)	14.72(15)
Na_2O	5.97(10)	5.99(15)	5.87(18)
K_2O	0.01(1)	0.03(5)	0.00(1)
Total	101.45(36)	100.93(39)	98.57(89)
Si	1.966(3)	1.961(2)	1.962(1)
Al	0.465(3)	0.466(2)	0.470(3)
Ti	0.003(1)	0.004(1)	0.003(1)
Cr	0.001(1)	0.001(1)	0.008(1)
Fe^{2+}	0.075(2)	0.076(3)	0.072(1)
Mn	0.000(0)	0.000(0)	0.001(1)
Mg	0.514(5)	0.516(5)	0.507(2)
Ca	0.571(5)	0.575(4)	0.567(1)
Na	0.404(6)	0.408(8)	0.409(9)
K	0.000(0)	0.002(2)	0.000(0)
Total	4.000(3)	4.007(3)	4.000(7)

712

This is the peer-reviewed, final accepted version for American Mineralogist, published by the Mineralogical Society of America.
The published version is subject to change. Cite as Authors (Year) Title. American Mineralogist, in press.
DOI: https://doi.org/10.2138/am-2023-9140. http://www.minsocam.org/

713 **Table 2**

Sample		Natural-8	Natural-11	Annealed-3	Annealed-7	Calculated (HF/DFT)
Space group		*P*2/*n*	*P*2/*n*	*C*2/*c*	*C*2/*c*	*P*2/*n*
Unit-cell parameters	*a* (Å)	9.5962(2)	9.5888(2)	9.6019(2)	9.5935(2)	9.614
	b (Å)	8.7897(2)	8.7852(2)	8.7781(3)	8.7725(2)	8.781
	c (Å)	5.2586(2)	5.2587(1)	5.2539(2)	5.2508(1)	5.287
	β (°)	106.789(2)	106.855(2)	106.692(2)	106.696(2)	107.22
	V (Å^3)	424.65(2)	423.96(2)	424.17(2)	423.27(2)	426.3

714

This is the peer-reviewed, final accepted version for American Mineralogist, published by the Mineralogical Society of America.
The published version is subject to change. Cite as Authors (Year) Title. American Mineralogist, in press.
DOI: https://doi.org/10.2138/am-2023-9140. http://www.minsocam.org/

715 **Table 3**

Sample		Natural-8	Natural-11			Annealed-3	Annealed-7
Space group		*P*2/*n*	*P*2/*n*			*C*2/*c*	*C*2/*c*
T1	Si	1.000(19)	1.000(18)	T	Si	0.9599(13)	0.9613(9)
	eps	14.000	14.000		Al	0.0401(13)	0.0387(9)
	eps_0	14.000	14.000		*eps*	13.96(3)	13.961(17)
<T1-O>		1.6338(8)	1.6330(8)		eps_0	14.000	14.000
T2	Si	0.9741(13)	0.9756(13)		<T-O>	1.6333(10)	1.6319(5)
	Al	0.0259(13)	0.0244(13)	M1	Mg	0.235(3)	0.802(2)
	eps	13.97(3)	13.98(3)		Al	0.728(2)	0.102(2)
	eps_0	14.000	14.000		Fe^{2+}	0.037(2)	0.096(2)
<T2-O>		1.6323(8)	1.6318(8)		*eps*	13.26(7)	13.43(5)
M1	Mg	0.882(2)	0.894(2)		eps_0	13.61(9)	13.56(9)
	Al	0.031(2)	0.015(2)		<M1-O>	2.0115(10)	2.0108(6)
	Fe^{2+}	0.087(2)	0.091(2)	M2	Ca	0.559(6)	0.560(3)
	eps	13.25(6)	13.30(7)		Na	0.441(6)	0.440(3)
	eps_0	13.31(7)	13.37(8)		*eps*	16.03(14)	16.04(7)
<M1-O>		2.0761(8)	2.0789(7)		eps_0	15.73(14)	15.65(12)
M11	Mg	0.100(2)	0.081(2)		<M2-O>	2.4892(10)	2.4871(5)
	Al	0.846(2)	0.867(2)				
	Fe^{2+}	0.054(2)	0.052(2)				
	eps	13.60(6)	13.59(6)				
	eps_0	13.52(7)	13.43(7)				
<M11-O>		1.9528(8)	1.9462(8)				
	Q_{M1}	0.828	0.864				
M2	Ca	0.3951(19)	0.3629(19)				
	Na	0.6049(19)	0.6370(19)				
	eps	14.56(5)	14.27(5)				
	eps_0	14.39(10)	13.97(12)				
<M2-O>		2.4725(8)	2.4714(8)				
M21	Ca	0.7801(19)	0.8034(19)				
	Na	0.2199(19)	0.1966(19)				
	eps	18.02(5)	18.23(5)				
	eps_0	17.86(10)	17.93(12)				
<M21-O>		2.5096(8)	2.5095(8)				
	Q_{M2}	0.397	0.453				

Note: *eps* = electron per site; eps_0 = electron per site, calculated without chemical constraints

716

This is the peer-reviewed, final accepted version for American Mineralogist, published by the Mineralogical Society of America.
The published version is subject to change. Cite as Authors (Year) Title. American Mineralogist, in press.
DOI: https://doi.org/10.2138/am-2023-9140. http://www.minsocam.org/

717 **Table 4**

	Calculated (HF/DFT)		Measured							
			Natural-8		Natural-11		Annealed-3		Annealed-7	
Mode	*ω*	*I*	*ω*	*I*	*ω*	*I*	*ω*	*I*	*ω*	*I*
A_g	142.34	10.69	146(1)	95.39	147(2)	44.38	146(1)	107.56	Not observed	
A_g	157.86	0.85	Not resolved		Not resolved					
A_g	190.94	5.63	194(3)	60.21	193(2)	18.97	189(1)	5.22	187(2)	1.72
A_g	215.48	6.47	220(3)	44.88	220(1)	77.24	225(2)	18.79	215(2)	67.30
A_g	229.60	1.67	238(2)	39.22	Not observed					
A_g	271.38	20.65	270(1)	27.57	271(1)	55.52	270(2)	2.32	267(1)	16.83
A_g	281.19	3.09	Not resolved		Not resolved					
A_g	300.37	5.72	301(2)	18.53	303(2)	16.88				
A_g	329.34	44.44	Not resolved		Not resolved					
A_g	337.48	123.53	335(1)	313.85	338(1)	293.94				
A_g	348.91	29.83	354(2)	202.48	Not resolved		350(1)	963.71	349(1)	190.36
A_g	375.24	43.96	Not resolved		372(1)	352.11				
A_g	381.97	130.59	380(1)	425.63	Not resolved		385(1)	175.16	382(2)	74.46
A_g	401.91	8.08	399(3)	348.59	397(2)	37.35				
A_g	410.63	136.60	414(1)	172.85	413(2)	86.02	410(1)	192.69	407(1)	94.08
A_g	452.38	0.88	Not resolved		Not resolved					
A_g	519.33	20.57	514(1)	6.32	516(1)	166.91	516(1)	65.84	513(2)	57.85
A_g	544.95	23.77	541(15)	210.92	541(1)	46.30				
A_g	562.54	51.87	563(1)	294.75	563(1)	217.96	561(1)	167.02	561(1)	145.63
A_g	609.11	49.85	595(2)	41.25	601(2)	14.54	594(2)	11.33	598(1)	19.62
A_g	688.08	1000.00	680(1)	1000.00	681(1)	1000.00	679(1)	1000.00	678(1)	1000.00
A_g	734.64	17.16	737(2)	3.28	734(2)	126.12				
A_g	899.22	35.84	882(2)	90.90	894(3)	133.15	877(2)	75.67	881(6)	41.35
A_g	916.33	78.28	911(2)	110.11	Not resolved		905(3)	90.16	906(8)	15.61
A_g	1007.44	601.98	1007(2)	508.12	1008(1)	608.87	1016(1)	424.02	1017(1)	946.97
A_g	1020.81	215.24	Not resolved		Not resolved					
A_g	1028.96	840.22	1023(2)	816.55	1026(1)	518.84				
A_g	1067.45	25.90	1096(2)	211.75	1076(3)	164.86				

Note: the calculated intensities correspond to polycrystalline material, whereas the listed experimental intensities for natural-8 and annealed-3 correspond to the square of (zz)-component of the Raman polarizabilty tensor measured in scattering geometry (**c** || $\mathbf{E}_i$ || $\mathbf{E}_s$), whereas the experimental intensities for natural-11 and annealed-7 correspond to a weighted sum of squared (xx)- and (yy)-components of the Raman polarizabilty tensor measured in scattering geometry (**c** $\perp$ $\mathbf{E}_i$ || $\mathbf{E}_s$), with weight coefficients depending on the **b**-axis orientation with respect to the laser-beam propagation (random in our study).

718

This is the peer-reviewed, final accepted version for American Mineralogist, published by the Mineralogical Society of America.
The published version is subject to change. Cite as Authors (Year) Title. American Mineralogist, in press.
DOI: https://doi.org/10.2138/am-2023-9140. http://www.minsocam.org/

719 **Table 5**

	Calculated (HF/DFT)	Pandolfo et al., 2012b	Pavese et al., 2001	Zhang et al., 2016
Di (wt%)	50.00	48.0	47.4	51.5
Jd (wt%)	50.00	52.0	46.4	46.5
Ae (wt%)	0.00	0.0	6.2	2.0
K_0 (GPa)	119(2)	122(1)	117(3)	116(2)
K'	4.9(5)	5.1(3)	6.0(1)	4.3(2)
V_0 (Å^3)	426.52(3)	421.43(4)	422.2(1)	423.9(3)
Q_{M1}	1	0.8956	0.84	0.81
Q_{M2}	1	0.4993	0.42	0.39
P (GPa)	0-6	0-7.5	0-13	0-47
T (°C)	25	25	25	25

Note: Q_{M1} and Q_{M2} of ordered omphacite are derived from ab initio simulations and experimentally determined in previous XRD studies (Di = diopside, Jd = jadeite, Ae = aegirine). For Zhang et al. (2016) Q_{M2} is calculated based on the site occupancy factor, while Q_{M1} as a function of the bond distances (Carpenter et al. 1990a).

720

This is the peer-reviewed, final accepted version for American Mineralogist, published by the Mineralogical Society of America.
The published version is subject to change. Cite as Authors (Year) Title. American Mineralogist, in press.
DOI: https://doi.org/10.2138/am-2023-9140. http://www.minsocam.org/

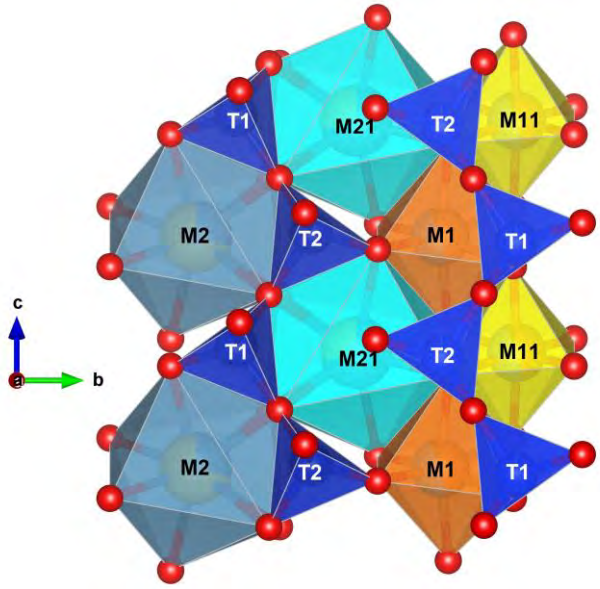

721

722 **Fig. 1**

This is the peer-reviewed, final accepted version for American Mineralogist, published by the Mineralogical Society of America.
The published version is subject to change. Cite as Authors (Year) Title. American Mineralogist, in press.
DOI: https://doi.org/10.2138/am-2023-9140. http://www.minsocam.org/

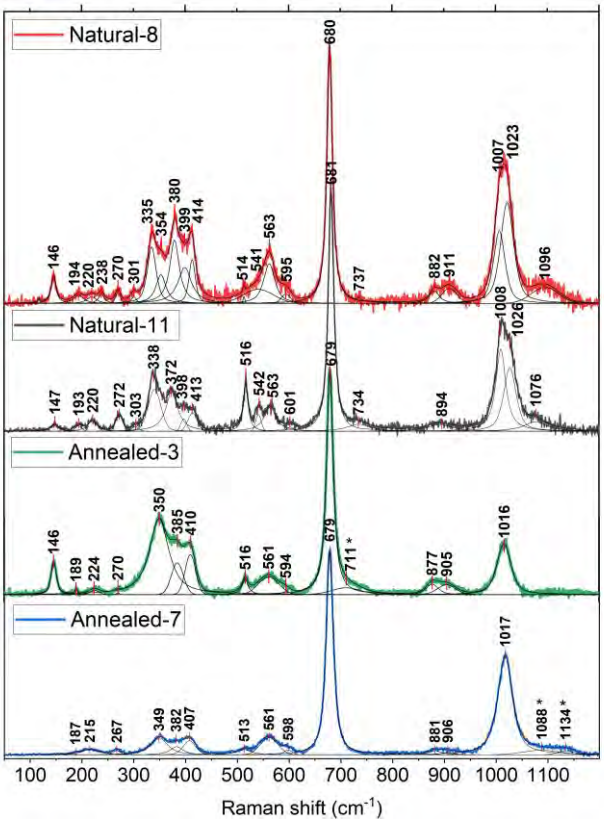

723

724 **Fig. 2**

This is the peer-reviewed, final accepted version for American Mineralogist, published by the Mineralogical Society of America.
The published version is subject to change. Cite as Authors (Year) Title. American Mineralogist, in press.
DOI: https://doi.org/10.2138/am-2023-9140. http://www.minsocam.org/

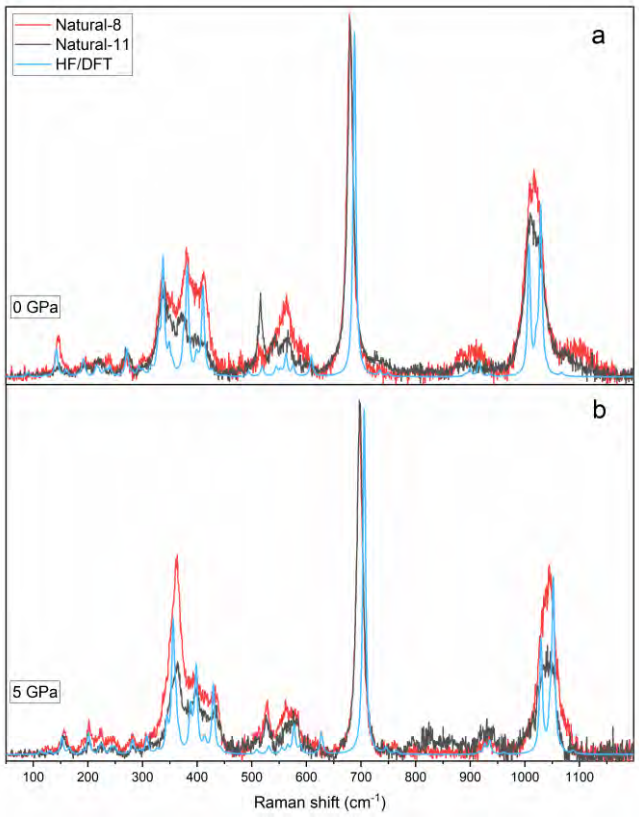

Fig. 3

This is the peer-reviewed, final accepted version for American Mineralogist, published by the Mineralogical Society of America.
The published version is subject to change. Cite as Authors (Year) Title. American Mineralogist, in press.
DOI: https://doi.org/10.2138/am-2023-9140. http://www.minsocam.org/

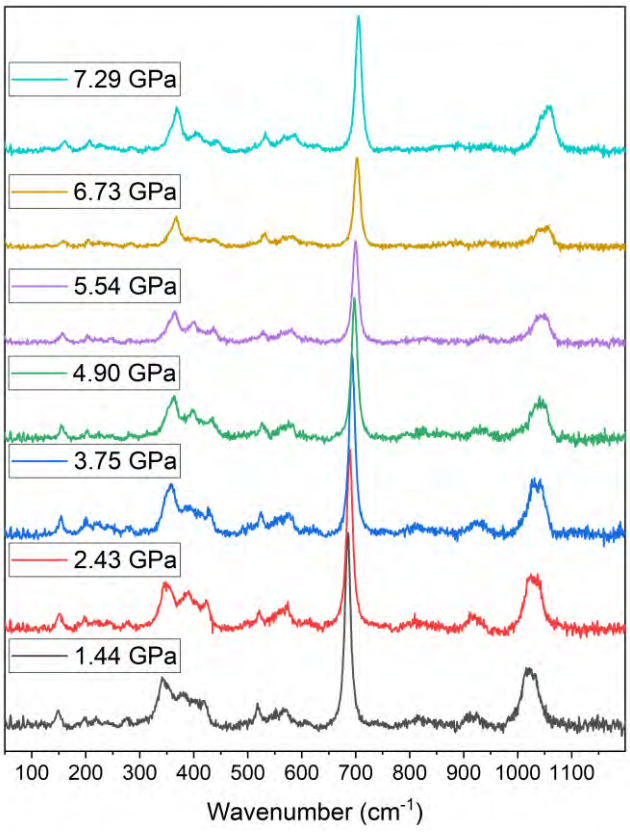

Fig. 4

This is the peer-reviewed, final accepted version for American Mineralogist, published by the Mineralogical Society of America.
The published version is subject to change. Cite as Authors (Year) Title. American Mineralogist, in press.
DOI: https://doi.org/10.2138/am-2023-9140. http://www.minsocam.org/

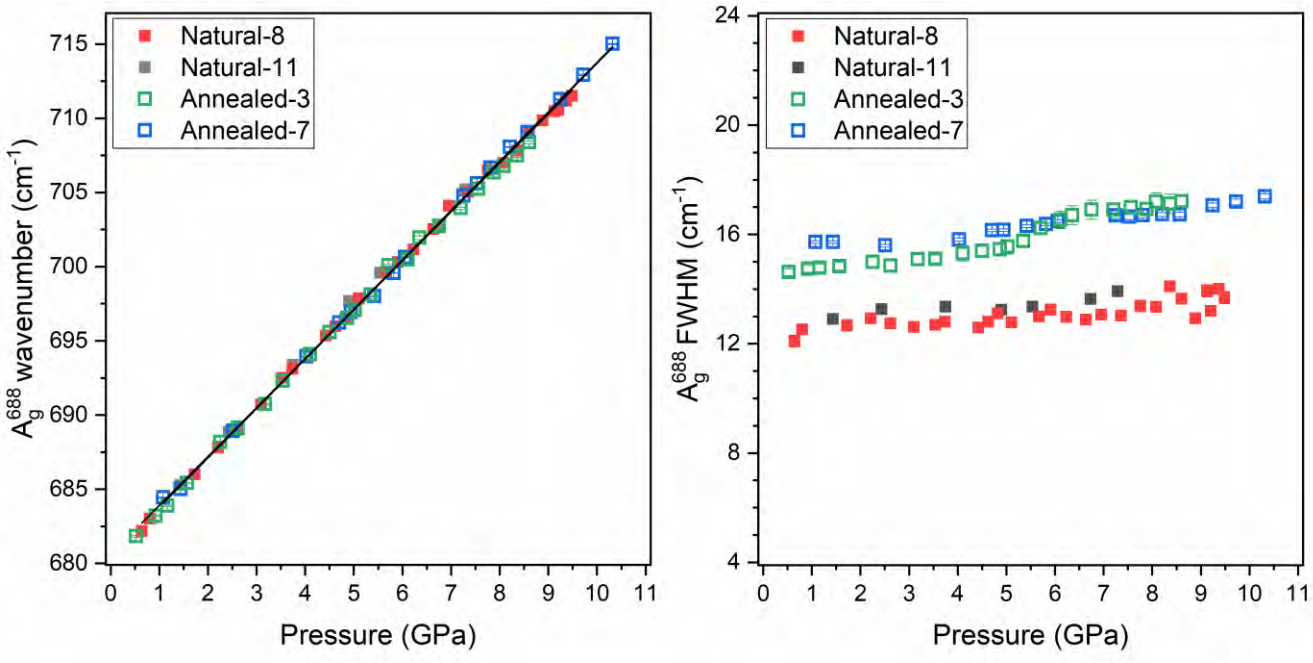

729

730 **Fig. 5**

This is the peer-reviewed, final accepted version for American Mineralogist, published by the Mineralogical Society of America.
The published version is subject to change. Cite as Authors (Year) Title. American Mineralogist, in press.
DOI: https://doi.org/10.2138/am-2023-9140. http://www.minsocam.org/

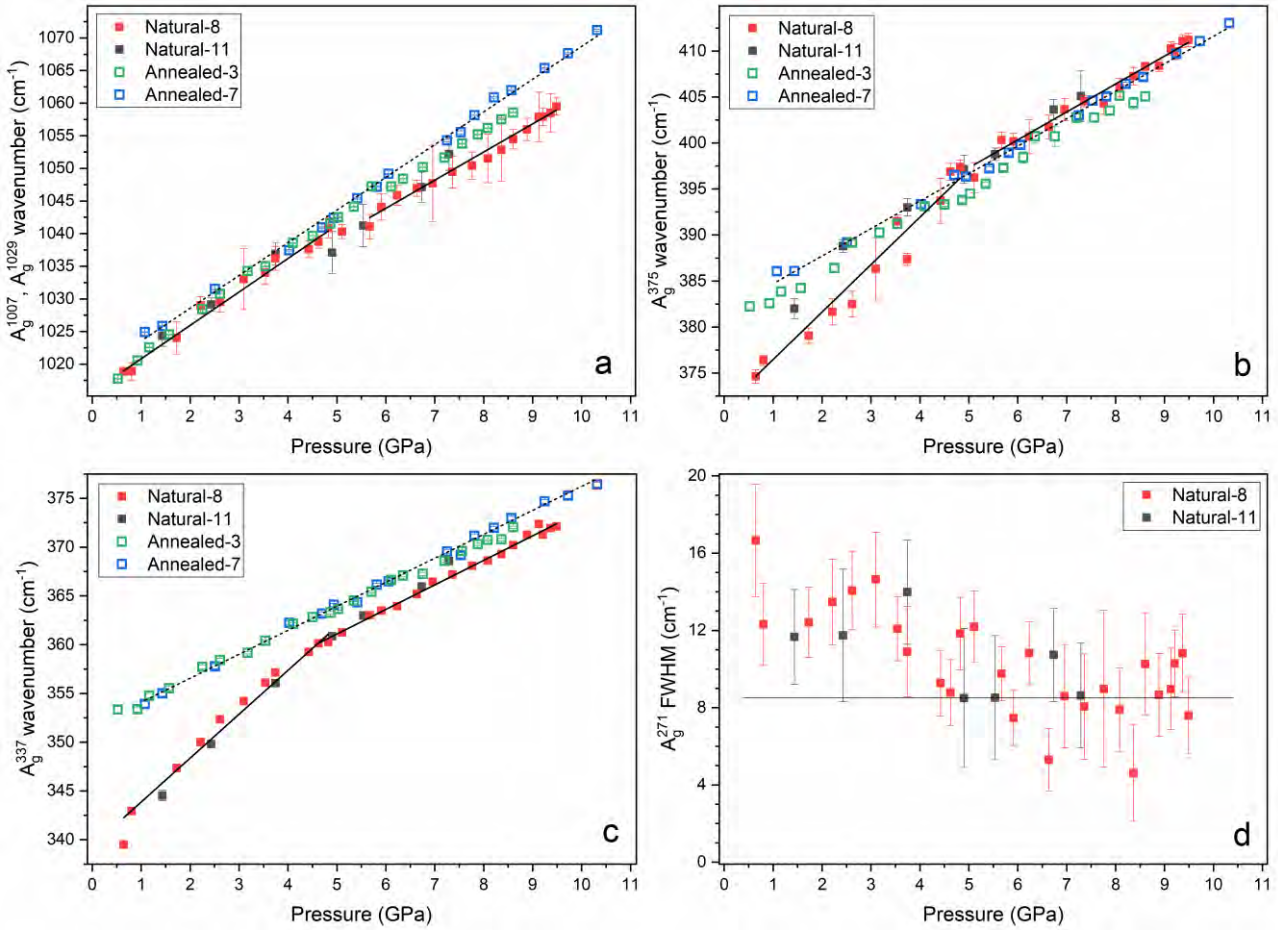

731

732 **Fig. 6**

This is the peer-reviewed, final accepted version for American Mineralogist, published by the Mineralogical Society of America.
The published version is subject to change. Cite as Authors (Year) Title. American Mineralogist, in press.
DOI: https://doi.org/10.2138/am-2023-9140. http://www.minsocam.org/

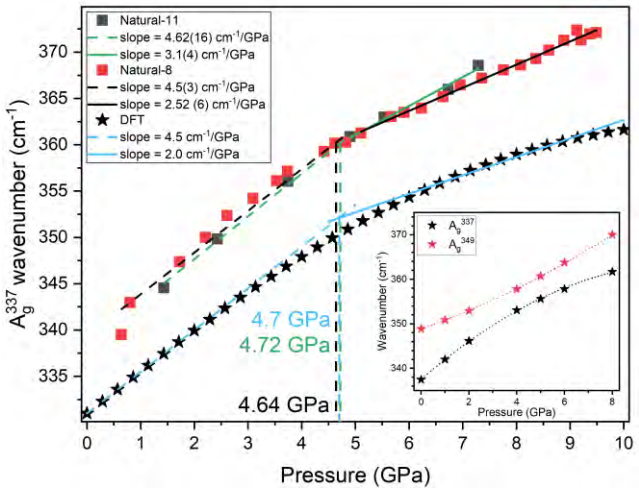

733

734 **Fig. 7**

This is the peer-reviewed, final accepted version for American Mineralogist, published by the Mineralogical Society of America.
The published version is subject to change. Cite as Authors (Year) Title. American Mineralogist, in press.
DOI: https://doi.org/10.2138/am-2023-9140. http://www.minsocam.org/

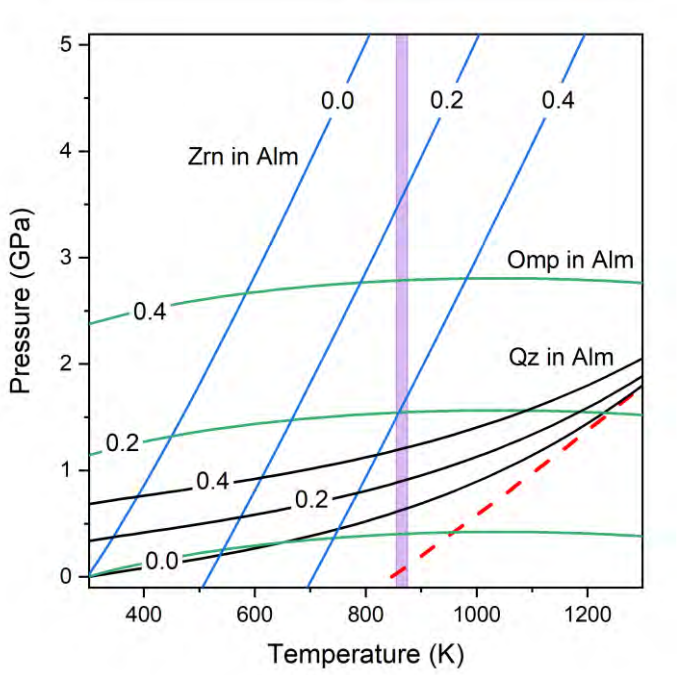

735

736 **Fig. 8**